

Synthesis, Morphology, and Magnetic Characterization of Iron Oxide Nanowires and Nanotubes

Lorenza Suber,^{*,†} Patrizia Imperatori,[‡] Giovanni Ausanio,[‡] Fabio Fabbri,[§] and Herbert Hofmeister^{||}

CNR-ISM, 00016 Monterotondo Stazione, Roma, Italy, INFM-Dipartimento Scienze Fisiche, Università di Napoli, Napoli, Italy, ENEA Frascati Research Center, 00044 Frascati, Roma, Italy, and MPI für Mikrostruktur Physik, 06120 Halle, Germany

Received: September 20, 2004; In Final Form: January 10, 2005

We have explored the synthesis of iron oxide particles, tubes, and fibrils within the pores of nanoporous polycarbonate and alumina membranes. The membranes contain uniformly distributed cylindrical pores with monodispersed diameters (varying between 20 and 200 nm) and thicknesses of 6 and 60 μm , respectively. By hydrolysis and polymerization of iron salts, particles of different sizes and phases were formed in the pores, building iron oxide particle nanowires. Alternatively, by the sol–gel technique, using as reagents metalloorganic compounds, fibrils and tubes of different iron oxide phases were prepared. Structural and morphological investigations performed using scanning electron microscopy and transmission electron microscopy revealed ordered iron oxide particle wires, tubes, and fibrils formed inside the membrane nanopores. Magnetic characterization was accomplished with a vibrating sample magnetometer. Below the blocking temperature (T_B), the magnetic behavior of the nanowires was governed by dipolar interaction between nearest-neighbor nanoparticles inside the pore, whereas the energy barrier, and therefore the T_B value, was mainly governed by dipolar interaction between magnetic moments over larger (interpore) distances. As expected, crystalline iron oxide nanotubes exhibited magnetic perpendicular anisotropy due to their magnetocrystalline and shape anisotropy.

1. Introduction

Materials based on the assembly of nanoparticles, nanotubes, and nanofibrils exhibit different electrical, magnetic, electro-optical, and chemical properties.¹

In the case of nanoparticles, their behavior arises from the large fraction of atoms which reside on their surface and from the finite number of atoms in each crystalline core. It was in magnetic materials² that such finite-size effects were first evidenced. Later, they were also noted in nonmagnetic materials such as semiconductors.^{3a,b}

Design of hollow tubular structures and particle nanowires has been the subject of considerable research in the past few years^{4–6} as these materials have shown their potential utility in a wide variety of chemical, biological, and materials science applications; the ability to assemble such materials with uniform and specified internal diameters into well-ordered superstructures is crucial for further developments. To this purpose, anodically grown alumina nanoporous membranes were used by Martin for preparing nanoscale tubes and fibrils.⁷ Solid or hollow microcylinders of desired materials, such as polymers,⁸ metals,⁹ and carbons, semiconductors, and metal oxides,¹⁰ have been obtained in the membrane pores, showing a number of interesting features. Particles too can be inserted easily into the pores, filling them and forming particle nanowires. A further advantage

of this method is that the material synthesized within the pores can then be freed from the membrane and collected, preserving, to a great extent, its superstructure.

Among the most interesting new aspects of monodimensional superstructures are their magnetic properties. Perpendicular magnetic media (with preferred magnetization perpendicular to the recording plane) is a field of great investigation. Magnetic media with perpendicular anisotropy allow a smaller bit size, and therefore, greater recording densities can be achieved.¹¹

We report on the preparation, structure, morphology, and magnetic properties of magnetite particle nanowires and iron oxide tubes and fibrils obtained in the pores of alumina and polycarbonate nanoporous membranes.

2. Experimental Section

The reagents iron(III) chloride (FeCl_3), iron(II) chloride (FeCl_2), tris(acetylacetonate)iron(III) ($\text{Fe}(\text{CH}_3\text{COCHCO}(\text{O}-)\text{CH}_3)_3$), and citric acid ($\text{HO}_2\text{CCH}_2\text{C}(\text{OH})(\text{CO}_2\text{H})\text{CH}_2\text{CO}_2\text{H}$) were purchased from Aldrich and used as received. Water PLUS for HPLC was purchased from Carlo Erba. Commercial alumina and polycarbonate nanoporous membranes were used: (alumina membranes) Whatman Anodisc 47, nominal pore diameter 20, 100, and 200 nm, pore density 1×10^9 pores/ cm^2 , membrane thickness 60 μm ; (polycarbonate membranes) Costar Nucleopore, nominal pore diameter 20 nm, pore density 6×10^8 pores/ cm^2 , membrane thickness 6 μm .

Bis(acetylacetonate)iron(II) ($\text{Fe}(\text{CH}_3\text{COCHCO}(\text{O}-)\text{CH}_3)_2$) was prepared under a N_2 atmosphere: Iron(II) chloride (4 g, 31 mmol) was dissolved in 6 mL of degassed water with gentle warming. A 9.17 mL sample of an ammonia solution (specific

* To whom correspondence should be addressed. E-mail: lorenza.suber@ism.cnr.it.

[†] CNR-ISM.

[‡] Università di Napoli.

[§] ENEA Frascati Research Center.

^{||} MPI für Mikrostruktur Physik.

gravity 0.892) was added slowly under stirring. The mixture was heated on a steam bath for 20 min, and the precipitate of iron(II) hydroxide was then filtered off and washed with degassed water until free from chloride. The moist iron(II) hydroxide and 7.3 mL of acetylacetone (specific gravity 0.976) were heated for 35 min. A light brown precipitate was obtained, which was dried under vacuum and recrystallized from ethanol.

Scanning electron microscopy (SEM) images of iron oxide tubes were obtained by dissolving the alumina membrane in a NaOH (5 N) solution, washing several times with distilled water, and drying. The sample was then coated by sputtering with gold. Transmission electron microscopy (TEM) investigations were performed by completely dissolving the polycarbonate membrane in CH_2Cl_2 and the alumina membranes in a NaOH (5 N) solution.

Powder X-ray diffraction (XRD) measurements were carried out in the 2θ range $25\text{--}80^\circ$ by means of an automated Seifert powder diffractometer using Cu K α radiation.

Magnetic measurements were carried out on a vibrating sample magnetometer (VSM Oxford Maglab9T).

Preparation of Samples. The samples were prepared by two different methods. Hematite and magnetite particle nanowires were prepared by method 1, whereas iron oxide tubes and fibrils were prepared by method 2.

Method 1: Particle Precipitation in Aqueous Solution. (S1) $\alpha\text{-Fe}_2\text{O}_3$ and $\beta\text{-FeOOH}$ Particle Nanowires. A 400 mL sample of an aqueous solution of 5.2×10^{-3} M FeCl_3 and 3.0×10^{-3} N HCl was heated to 60°C . A polycarbonate nanoporous membrane (pore diameter 20 nm) was immersed in the solution, and the reaction was refluxed for 3 days, whereby a precipitate was formed. The temperature was decreased to 25°C , and the membrane was washed three times with water to eliminate extraneous ions and dried. The precipitate was filtered off, washed three times with water, and dried.

(S2) $\gamma\text{-FeOOH}$ Particle Nanowires. A 200 mL sample of an aqueous solution of 1.02×10^{-2} M FeCl_3 and 2.63×10^{-4} M NaH_2PO_4 was heated to 50°C . A polycarbonate nanoporous membrane (pore diameter 20 nm) was immersed in the solution, and the reaction was refluxed for 6 days, whereby a precipitate was formed. The rest of the procedure is the same as that for S1.

(S3) Magnetite Particle Nanowires. The reaction was performed in a N_2 atmosphere. An alumina membrane (pore diameter 20 nm) was immersed in a 50 mL aqueous solution of 0.5 M $(\text{CH}_3)_4\text{NNO}_3$. Then 5 mL of an aqueous solution of 1×10^{-1} M FeCl_2 and 2×10^{-1} M FeCl_3 was added dropwise, the pH being maintained at a constant value of 12 by dropwise addition of a 2.8 M $(\text{CH}_3)_4\text{NOH}$ solution.¹² A black precipitate was formed. The precipitate was digested under mechanical stirring for 4 days at 25°C . The membrane was then washed three times with degassed water to eliminate extraneous ions and dried under vacuum.

Method 2: Sol-Gel Synthesis. (S4) Amorphous Iron Oxide Tubes. An alumina membrane (pore diameter 200 nm) was immersed in 50 mL of an ethyl alcohol solution of 5×10^{-3} M iron(III) acetylacetonate and 2×10^{-2} M citric acid. The solution was evaporated at room temperature overnight, forming a gel. The membrane was dried at 60°C for 4 h, then thermally treated in a muffle at 460°C for 12 h by increasing the temperature at a rate of $1^\circ\text{C}/\text{min}$, and then cooled to room temperature at a rate of $1^\circ\text{C}/\text{min}$.

(S5) Amorphous Iron Oxide Fibrils. A procedure like the above except that an alumina membrane with a pore diameter of 100 nm was used.

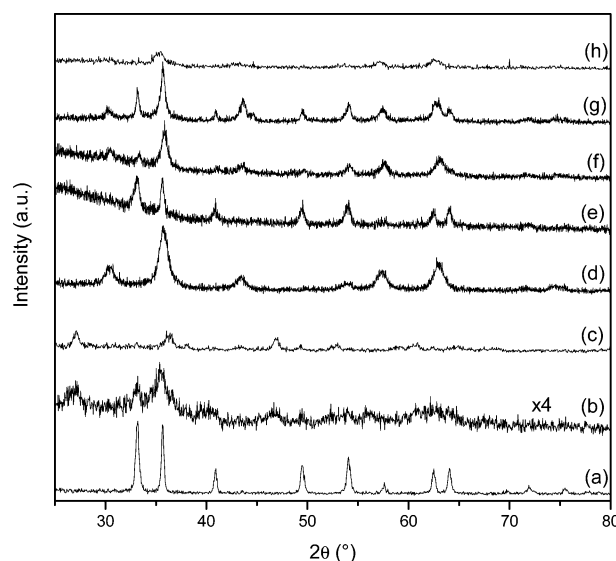


Figure 1. XRD patterns of (a) $\alpha\text{-Fe}_2\text{O}_3$ particles, (b) $\alpha\text{-Fe}_2\text{O}_3$ and $\beta\text{-FeOOH}$ particles, (c) $\gamma\text{-FeOOH}$ particles, (d) Fe_3O_4 nanoparticles, (e) $\alpha\text{-Fe}_2\text{O}_3$ tubes treated at 600°C (S6), (f) $\gamma\text{-Fe}_2\text{O}_3$ formed outside the pores for treatments up to 270°C , (g) $\alpha\text{-Fe}_2\text{O}_3$ and $\gamma\text{-Fe}_2\text{O}_3$ phases formed at 300°C , and (h) $\gamma\text{-Fe}_2\text{O}_3$ tubes after thermal treatment at 270°C (S7).

(S6) Hematite ($\alpha\text{-Fe}_2\text{O}_3$) Wires. An alumina membrane (pore diameter 200 nm) was immersed in 50 mL of an ethyl alcohol solution of 5×10^{-3} M iron(III) acetylacetonate and 2×10^{-2} M citric acid. The solution was evaporated at room temperature overnight, forming a gel. The membrane was thermally treated at 60°C for 4 h and then in a muffle at 100°C for 4 h, whereby the temperature was increased, at a rate of $1^\circ\text{C}/\text{min}$, to 400°C . After 12 h at 400°C , the temperature was increased, at a rate of $1^\circ\text{C}/\text{min}$, to 600°C . After 12 h at 600°C , the temperature was decreased, at a rate of $1^\circ\text{C}/\text{min}$, to 25°C .

(S7) Maghemite ($\gamma\text{-Fe}_2\text{O}_3$) Tubes. The preparation was performed under a N_2 atmosphere. An alumina membrane (pore diameter 200 nm) was immersed in 50 mL of a degassed ethyl alcohol solution constituted by 5×10^{-3} M iron(II) acetylacetonate and 2×10^{-2} M citric acid. The solution was left at room temperature overnight. The ethyl alcohol was then evaporated at 60°C under reduced pressure, whereby a gel was formed. The membrane was then dried at 60°C for 4 h and thermally treated. The temperature was increased at a rate of $1^\circ\text{C}/\text{min}$ to 200°C and after 1 h increased to 270°C for 24 h. The temperature was then decreased at a rate of $1^\circ\text{C}/\text{min}$ to room temperature. The precipitate formed outside the membrane pores was dried and thermally treated as above.

Finally, all the samples were lapped with SBT (South Bay Technology Inc.) 1200 grit silicon carbide paper to remove iron oxide formed outside the pores on the membrane surfaces.

3. Results and Discussion

Scanning electron micrographs of the polycarbonate and alumina nanoporous host membranes confirmed the nominal pore diameters of 20, 100, and 200 nm.

By hydrolysis and polymerization of iron chloride in strongly acidic conditions, a precipitate constituted by almost spherical hematite ($\alpha\text{-Fe}_2\text{O}_3$) particles was formed. In the XRD spectrum shown in Figure 1a only the hematite peaks were present, and by application of Scherrer's equation,¹³ a crystallite size of about 30 nm was estimated.

When the same reaction was performed in the membrane nanopores, by immersing the membrane in the reaction solution,

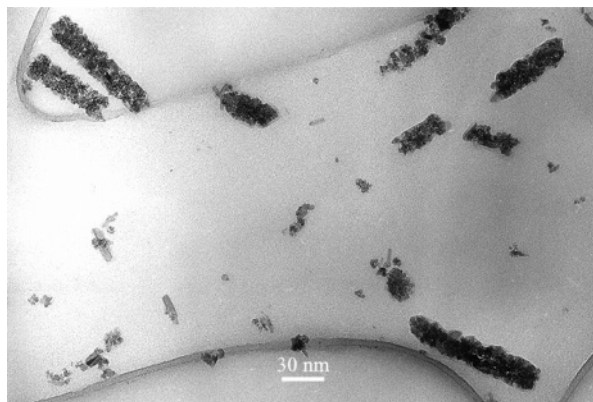


Figure 2. BF TEM micrograph of particle nanowires (S1) formed by rod-shaped akaganeite (β -FeOOH) and spherical hematite (α -Fe₂O₃) particles.

a mixture of hematite and akaganeite (β -FeOOH) particles were formed in the nanopores, as shown by XRD (Figure 1b). From a Rietveld quantitative analysis of the XRD data,¹⁴ we determined a ratio of approximately 30% hematite to 70% akaganeite. In these reaction conditions, the β -FeOOH phase crystallizes in the rod-shaped morphology, whereas α -Fe₂O₃ spherical particles are formed (see below) as also evidenced by transmission electron microscopy (Figure 2).

Furthermore, if the membrane is immersed in a solution of iron chloride and monobasic sodium phosphate, *only* rod-shaped lepidocrocite (γ -FeOOH) particles are formed, either in the membrane pore or in the precipitate, as evidenced by XRD (Figure 1c) and TEM measurements.

In the first case, the presence of both the α -Fe₂O₃ phase and the β -FeOOH phase inside the pores is attributable to the constrained reaction space in the 20 nm diameter pores, which partially hinders the transformation of the β -FeOOH phase to the α -Fe₂O₃ phase. This supports the hematite formation mechanism hypothesis,¹⁵ i.e., that β -FeOOH particles are initially formed and then dissolve to yield the more stable hematite particles.

Analogously, in the second case we were expecting the formation of acicular hematite particles in the precipitate formed outside the pores, as reported in the literature,¹⁶ and also of the lepidocrocite phase inside the pores. On the contrary, we observed, both inside and outside the pores, only the formation of γ -FeOOH particles. In this case, a possible explanation is that the reagent NaH₂PO₄, responsible for the formation of the acicular hematite particles through coordination of the PO₄³⁻ to preferential iron oxide crystalline planes, may instead be mainly adsorbed on the alumina membrane itself. Once absorbed on the membrane, it could favor the formation of the lepidocrocite phase at the solid–liquid interface. An analogous effect was hypothesized by Nagtegaal et al.¹⁷ for the formation of lepidocrocite on sulfonated functionalized surfaces.

In the case of the reaction of ferrous and ferric salts (1:2) inside the membrane pores, magnetite particles were formed (S3), as evidenced by their XRD spectrum (Figure 1d) and by the chemical determination of the Fe³⁺:Fe²⁺ ratio (close to 2:1 as expected for magnetite).¹⁸ The particle mean diameter deduced by X-ray diffraction data (Scherrer's equation) was 9 nm. TEM measurements (Figure 3) showed, besides isolated particles, bundles of a few particle nanowires. The length of the nanowires is shorter than expected due to their thinness and the drastic conditions used to dissolve the template membrane.

The precipitation method turned out to be very efficient in the preparation of particle nanowires but unsuitable for the



Figure 3. TEM negative micrograph of magnetite particle nanowires (S3).

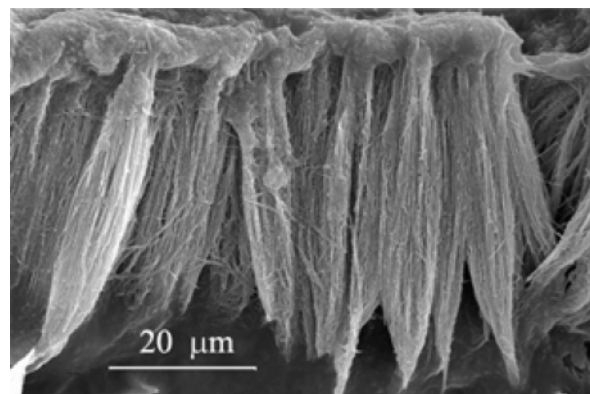
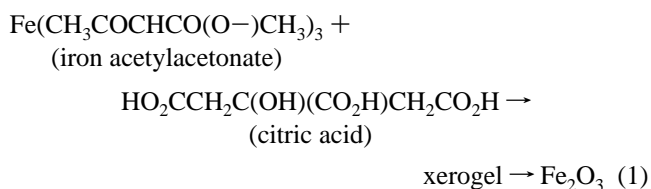


Figure 4. SEM micrograph of amorphous iron oxide fibrils *partially* freed from the template membrane (S5). Only one face of the membrane was lapped. The iron oxide present on the unlapped surface keeps all the fibrils tied together.

preparation of tubelike structures. To this purpose, the sol–gel method is indicated.

Iron oxide tubes (S4) and fibrils (S5) were formed via the *sol–gel* method, by reaction of iron acetylacetonate and citric acid (eq 1) and subsequent thermal treatment at 400 °C for 12 h.



XRD measurements showed the iron oxide tubes (S4) and fibrils (S5) to be amorphous. For clarity the spectra are not included in Figure 1. Morphological investigations by SEM, after the fibrils were freed from the alumina membrane by dissolving it in a 10 N NaOH solution, showed an ordered assembly of fibrils (Figure 4).

When using the membrane with a pore diameter of 100 nm, iron oxide fibrils were formed (S5), while the same procedure

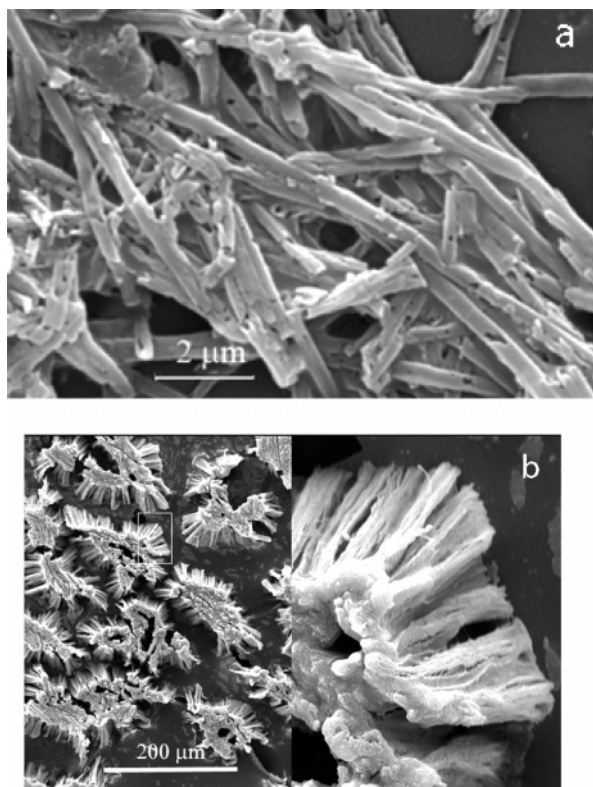


Figure 5. (a) SEM micrograph of amorphous iron oxide tubes completely freed from the template membrane (S4). (b) SEM micrograph of amorphous iron oxide tubes, partially freed from the template membrane (one side of the membrane has not been lapped).

applied to an alumina membrane with a pore diameter of 200 nm led to the formation of iron oxide tubes as shown by SEM micrographs (Figure 5).

Figure 5a in particular, showing iron oxide tubes with holes on their walls caused by the drastic conditions used to dissolve the membrane, represents clear evidence of the tubelike iron oxide superstructure. Iron oxide tubes are formed most probably because the alumina pore walls with their OH^- groups favor electrostatically the coordination of iron cations and therefore the formation, by subsequent polymerization, of the iron oxide layer around the alumina pore walls. Depending on the reaction time and on the pore diameter, the tubes can be filled and fibrils are formed. In our case, as the reaction time is the same in both cases, the different pore diameters (100 and 200 nm) are the main factor causing the formation of iron oxide fibrils and tubes, respectively. In the first case, to observe the formation of iron oxide tubes, a shorter reaction time would be necessary, whereas, in the second case, to obtain iron oxide fibrils, a longer reaction time would be required.

XRD data of the iron oxide tubes thermally treated at 460 °C evidenced poor crystallinity. To favor the formation of a crystalline phase, the annealing process was increased to 600 °C (S6). At this temperature the $\alpha\text{-Fe}_2\text{O}_3$ phase appeared as shown in the XRD pattern (Figure 1e). TEM measurements evidenced the formation of spherical particles with a mean diameter of 100 nm (Figure 6). SAED (selected area electron diffraction) shown in the inset confirmed the formation of the hematite phase, the rings being indexed according to the rhombohedral hematite structure (72-469 JCPDS-ICDD).

The formation of the hematite phase was also confirmed by magnetization measurements (see below). Finally, to obtain maghemite ($\gamma\text{-Fe}_2\text{O}_3$) nanotubes, reactions using bis(acetylacetonate)iron(II) as the metalloorganic precursor were performed.

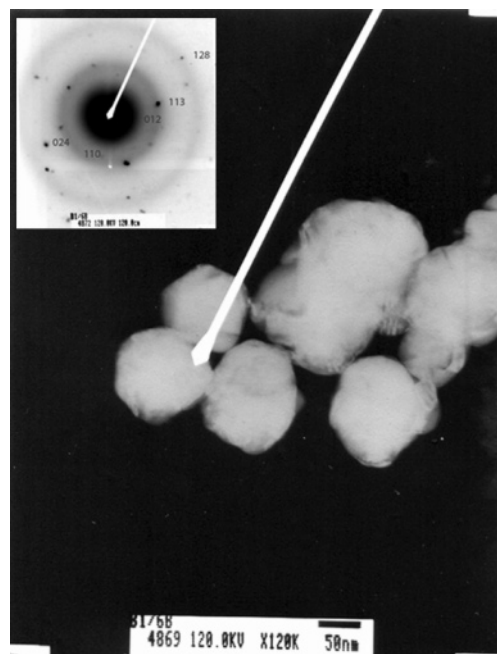


Figure 6. TEM and SAED (electron diffraction of selected area, inset) micrographs of S6 indicating a polycrystalline hematite phase

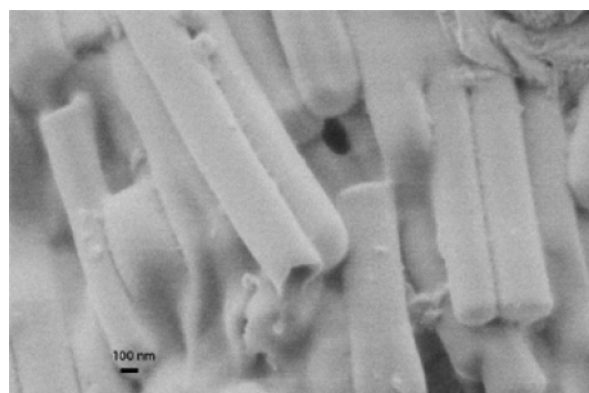


Figure 7. SEM micrograph of iron oxide tubes (S7) after thermal treatment at 270 °C.

Annealing treatments up to 270 °C revealed the formation, outside the pores, of maghemite particles as shown by XRD measurements (Figure 1f). The diameter of the particles estimated by Scherrer's equation was 10 nm. Above 270 °C, we noted the initial formation of the more stable hematite phase. As an example, the data for the sample treated at 300 °C are reported in Figure 1g. The Rietveld quantitative analysis of the XRD data showed relative amounts of approximately 50% for each phase (hematite and maghemite).

SEM micrographs of the material formed inside the pores showed iron oxide tubes (Figure 7). The presence of iron was also confirmed by EDS measurements.

X-ray diffraction data of the iron oxide tubes thermally treated at 270 °C (S7) still indicated poor crystallinity. The broad peaks are attributable to the maghemite phase (Figure 1h). Higher annealing temperatures were not attempted because of the probable formation of the more stable $\alpha\text{-Fe}_2\text{O}_3$ phase.

Experimentally, the perpendicular magnetization of nanowires and nanotubes can be ascertained by magnetometry measurements with the external field applied perpendicular to the membrane plane (hence parallel to the nanowire or nanotube main axis) and parallel to the membrane plane (hence perpendicular to the nanowire or nanotube main axis).

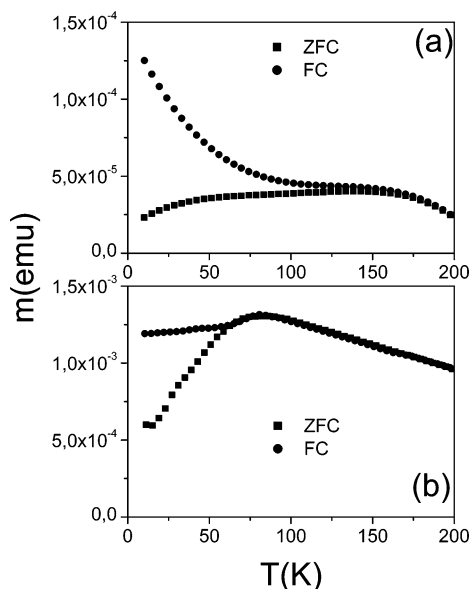


Figure 8. Temperature dependence of ZFC and FC magnetization of nanowires of magnetite particles (S3) for the magnetic field $\mu_0\mathbf{H} = 10$ mT aligned (a) perpendicular and (b) parallel to the main axis of the wire.

Measurements of magnetization versus temperature were performed using standard experimental zero-field cooling and field cooling protocols, with the magnetic field, $\mu_0\mathbf{H}$, aligned both parallel and perpendicular to the nanowire or nanotube long axis.

In the case of magnetite particles nanowires (S3), magnetization versus temperature measurements were performed with the magnetic field $\mu_0\mathbf{H} = 10$ mT (Figure 8). The curves show the typical features (maximum of ZFC magnetization, low-temperature splitting between FC and ZFC curves) of an assembly of magnetic nanoparticles presenting a volume (V) distribution, implying a distribution of anisotropy energy barriers E_B (where $E_B = K_a V$ for uniaxial anisotropy; K_a = anisotropic constant).¹⁹ For noninteracting particle systems, the temperature of the ZFC maximum (T_{\max}) is found to increase with the particle size and, in general, is related to the average blocking temperature $\langle T_B \rangle$, according to relationships that depend on the volume distribution function.²⁰ The particle moments thermally fluctuate freely in the high-temperature superparamagnetic state and are blocked below the average blocking temperature $\langle T_B \rangle$. Using the relation $T_B = K_a V / 25 K_b$ (where K_a = anisotropic constant and K_b = Boltzmann constant) for uniaxial *noninteracting* magnetite particles with a diameter of 10 nm,²¹ T_B is found to be 20 K.

In the case of *interacting* particle systems, on the other hand, the effect of dipolar interaction is to increase the blocking temperature T_B , related to T_{\max} , due to enhanced energy barriers.²² In our system, T_{\max} depends also on the dipolar interaction between the *neighbor* nanopore magnetic moments (the mean distance between nanopores is 20 nm), which is the sum of the nanoparticle magnetic moments in the single nanopore. So, when the magnetic field is applied parallel to the nanowire long axis (Figure 8b), the nanopores' magnetic moments being in an unstable arrangement and therefore interacting weakly, T_{\max} is 80 K, whereas, when the magnetic field is applied perpendicular to the long axis, T_{\max} increases to 125 K (Figure 8a).

Below T_{\max} , a difference is observed in the FC magnetization behavior for a magnetic field applied parallel or perpendicular to the nanowire long axis. In the first case, when the magnetic field is applied perpendicular to the nanowire axis (Figure 8a),

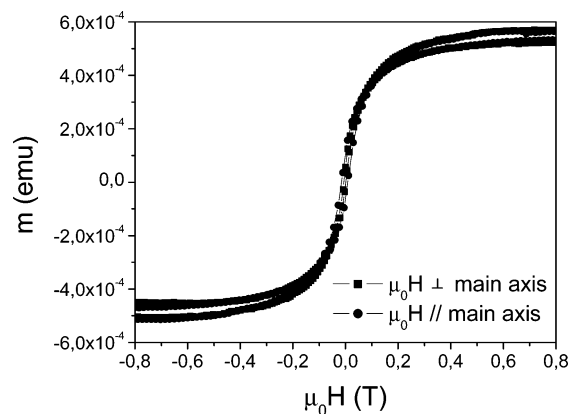


Figure 9. Hysteresis loops at $T = 200$ K of magnetite particle wires (S3) with the magnetic field aligned both perpendicular and parallel to the main axis of the wire.

a Curie-like behavior is observed, indicating that the sample consists of noninteracting or very weakly interacting particles, whereas, in the second case, when the magnetic field is applied parallel to the nanowire long axis (Figure 8b), the magnetization shows a plateau. This behavior is usually observed in strongly interacting particles, such as spin glasses, where a collective moment blocking can be observed.²³ Actually, the dipolar interaction between the magnetic moments of two particles depends on the relative orientation of the two moments as well as on their orientation, relative to the vector joining the two moments' sites. When the magnetic field is applied perpendicular to the nanowire long axis, the nanoparticle magnetic moments are parallel to each other, but in an unstable arrangement, and therefore, they weakly interact. Conversely, when the magnetic field is applied parallel to the nanowire long axis, the nanoparticle magnetic moments are still parallel but in a stable arrangement; therefore, they strongly interact.

At 200 K, i.e., above T_{\max} , a hysteretic behavior was observed (Figure 9), denoting a fraction of aggregated particles inside the membrane pores. Aggregation of small particles causing a hysteretic behavior above T_{\max} has been previously reported in the literature.²⁴ The shapes of the hysteresis loops measured with the magnetic field aligned both parallel and perpendicular to the long axis of the wires are quite similar, indicating no observable anisotropy as expected for a system constituted by almost spherical nanoparticles. The increased H_c value of 100 Oe, obtained for the magnetic field applied parallel to the pore long axis, compared to the 40 Oe for the magnetic field applied perpendicular to the pore long axis at 200 K, is in agreement with a stronger dipole interaction as observed in the respective T_{\max} values (see Figure 8).

Due to their shape anisotropy, iron oxide tubes evidenced the existence of a perpendicular magnetic anisotropy. Figure 10 in fact shows the hysteresis loops at $T = 200$ K obtained for $\gamma\text{-Fe}_2\text{O}_3$ tubes (S7), when the applied external magnetic field is parallel and perpendicular to the nanotube long axis. The different curves clearly indicate the existence of a perpendicular magnetic anisotropy. This is also true if magnetic saturation is not reached (magnetic field $\mu_0\mathbf{H} = 5$ T), maybe due to the magnetocrystalline anisotropy in competition with the shape anisotropy.

Actually, if the reduced hysteresis loop is compared to that of the S4 sample (Figure 11), it is observed that, in the latter, the magnetization saturation occurs at an applied field $\mu_0\mathbf{H} = 3$ T. Being completely amorphous, it has lower magnetocrystalline anisotropy than the S7 sample, and therefore, only shape magnetic anisotropy is present. Moreover, in the S4 sample,

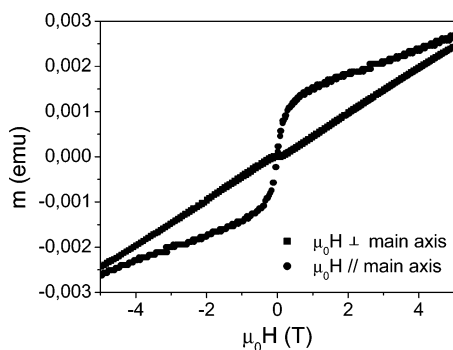


Figure 10. Hysteresis loops for tubes $\gamma\text{-Fe}_2\text{O}_3$ (S7) at $T = 200$ K with the magnetic field aligned both perpendicular and parallel to the main tube axis.

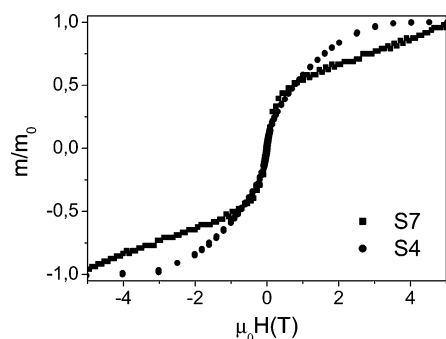


Figure 11. Reduced hysteresis loops for the iron oxide tubes S4 and S7 with the applied field parallel to the nanotube main axis. The total magnetic moment at the maximum applied field is m_0 .

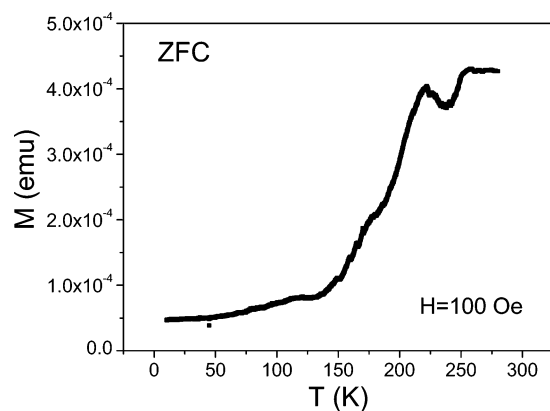


Figure 12. Magnetization versus temperature for sample S6, in a magnetic field $\mu_0\mathbf{H} = 10$ mT aligned parallel to the nanotube main axis.

magnetization approaches the saturation value mainly by rotation of the domain magnetization. The magnetization rotation occurs in a system characterized by the absence of domain walls, and again this happens in a material with low magnetocrystalline anisotropy.

The temperature dependence of the magnetization in a magnetic field $\mu_0\mathbf{H} = 10$ mT for sample S6, applied along the nanowires main axis, is shown in Figure 12. A spin-flip magnetic transition at $T_M = 225$ K, the so-called Morin point, is observed. The bulk hematite is weakly ferromagnetic at high temperature, $T > 263$ K, with the magnetically ordered spins lying in the plane perpendicular to the [111] axis (*c*-axis) except for a slight spin canting (~ 1 min of arc) out of the plane, which gives rise to the small net weak ferromagnetic moment. It becomes antiferromagnetic below $T = 263$ K, the Morin temperature, when the magnetically ordered spins become

aligned with the trigonal [111] (*c*-axis).²⁵ The Morin temperature depends, among other parameters, on particle size; actually it decreases with decreasing size, disappearing when the particle diameter is below 8 nm, where a superparamagnetic behavior is observed. From TEM measurements, the estimated mean diameter of the S6 hematite particles was 100 nm.

4. Conclusions

Nanoporous membranes are formidable templating agents for the preparation, by chemical methods, of well-ordered magnetic nanowires, nanofibrils, and nanotubes.

Magnetic nanowires, constituted by magnetite nanoparticles with mean diameters of 9 nm, were prepared by precipitation of iron(II) and iron(III) salts inside the membrane nanopores. Magnetization measurements indicated a magnetic behavior governed, below the blocking temperature (T_B), by the dipolar interaction among nearest nanoparticles inside the nanopore, whereas the energy barrier, and therefore T_B value, was determined mainly by dipolar interactions among magnetic moments, interacting at larger distances (with magnetic moments located in the neighboring nanopores).

Amorphous iron(III) oxide tubes and fibrils were prepared by the sol–gel method. Hematite tubes constituted by crystalline nanoparticles were obtained by thermal treatment of the amorphous phase at 600 °C, as shown by TEM electron diffraction measurements and the appearance of the Morin transition in the ZFC magnetization curve. This was not observed in the iron oxide tubes, treated at lower temperatures.

Thermal treatments performed at 270 °C on amorphous iron-(II,III) oxide tubes instead led to a poorly crystalline $\gamma\text{-Fe}_2\text{O}_3$ phase.

Acknowledgment. We thank Dr. Stefano Martelli, Dino Fiorani and Prof. Luciano Lanotte for their interest and help with the experiments and Mr. William R. Plunkett for revision of the language.

References and Notes

- (1) (a) Sundaram, M.; Chalmeras, S. A.; Hopkins, P. F.; Gossard, A. C. *Science* **1991**, 254, 1326. (b) Niemeyer, C. M. *Angew. Chem., Int. Ed.* **2001**, 40, 4128.
- (2) Martín, J. I.; Nogués, J.; Liu, K.; Vincent, J. L.; Schuller, I. K. *J. Magn. Mater.* **2003**, 256, 449 and references therein.
- (3) (a) Murray, C. B.; Norris, D. J.; Bawendi, M. G. *J. Am. Chem. Soc.* **1993**, 115, 8706. (b) Murray, C. B.; Kagan, C. R.; Bawendi, M. G. *Science* **1995**, 270, 1335. (c) Foglia, S.; Suber, L.; Righini, M. *Colloids Surf., A* **2001**, 177, 3.
- (4) Iijima, S. *Nature* **1991**, 354, 56.
- (5) Nakamura, H.; Matsui, Y. *Adv. Mater.* **1995**, 7, 871.
- (6) (a) Orr, G. W.; Barbour, L. J.; Atwood, J. L. *Science* **1999**, 285, 1049. (b) Wang, G.; Hollingsworth, R. I. *Langmuir* **1999**, 15, 6135. (c) Suber, L.; Foglia, S.; Chiozzini, G. In *Conference Proceedings, 74, Nanotubes and Nanostructures 2000*; Bellucci, S., Ed.; SIF: Bologna, 2001. (d) Yan, D.; Zhou, Y.; Hou, J. *Science* **2004**, 303, 65. (e) Rao, C. N. R.; Deepak, F. L.; Gundiah, G.; Govindaraj, A. *Prog. Solid State Chem.* **2003**, 31, 5. (f) Wei, Z.; Zhang, Z.; Wan, M. *Langmuir* **2002**, 18, 917.
- (7) (a) Martin, C. R.; Van Dyke, L. S.; Cai, Z.; Liang, W. *J. Am. Chem. Soc.* **1990**, 112, 8976. (b) Martin, C. R. *Adv. Mater.* **1991**, 3, 457. (c) Martin, C. R. *Science* **1994**, 266, 1961. (d) Martin, C. R. *Chem. Mater.* **1996**, 8, 1739. (e) Cepak, V.; Hulthen, J. C.; Che, G.; Jirage, K. B.; Lakshmi, B. B.; Fisher, E. R.; Martin, C. R. *Chem. Mater.* **1997**, 9, 1065.
- (8) Martin, C. R. *Acc. Chem. Res.* **1995**, 28, 861.
- (9) (a) Zhang, Z.; Dai, S.; Blom, D. A.; Shen, J. *Chem. Mater.* **2002**, 14, 965. (b) Yu, J.; Kim, J. Y.; Lee, S.; Mbindyo, J. K. N.; Martin, B. R.; Mallouk, T. E. *Chem. Commun.* **2000**, 2445.
- (10) (a) Parthasarathy, R. V.; Phani, K. L. N.; Martin, C. R. *Adv. Mater.* **1995**, 7, 896. (b) Liu, S. M.; Gan, L. M.; Zhang, W. D.; Zeng, H. C. *Chem. Mater.* **2002**, 14, 1391 and references therein.
- (11) (a) Ji, G.; Tang, S.; Xu, B.; Gu, B.; Du, Y. *Chem. Phys. Lett.* **2003**, 379, 484, and refs therein. (b) Yang, Y. W.; Meng, G. W.; Liang, C. H.;

- Wang, G. Z.; Zhang, L. D. *Chem. Phys. Lett.* **2001**, 339, 174. (c) Khan, H. R.; Petrikowski, K. *J. Magn. Magn. Mater.* **2002**, 249, 458. (d) Skomski, R.; Zeng, H.; Sellmyer, D. J. *J. Magn. Magn. Mater.* **2002**, 249, 175. (e) Martin, J. I.; Vélez, M.; Morales, R.; Alameda, J. M.; Anguita, J. V.; Briones, F.; Vicent, J. L. *J. Magn. Magn. Mater.* **2002**, 249, 156.
- (12) Vayssières, L.; Chanéac, C.; Tronc, E.; Jolivet, J. P. *J. Colloid Interface Sci.* **1998**, 205, 205.
- (13) Cornell R. M. In *The Iron Oxides, 7U*; Schwertmann, Ed.; Wiley-VCH: Weinheim, Germany, 1996.
- (14) Bish, D. L.; Post, J. E., Eds. *Modern Powder Diffraction; Reviews in Mineralogy*; The Mineralogical Society of America: Washington, DC, 1989; Vol. 20.
- (15) Morales, M. P.; Gonzáles-Carreno, T.; Serna, C. J. *J. Mater. Res.* **1992**, 7, 2538 and references therein.
- (16) Ozaki, M.; Krathovil, S.; Matijević, E. *J. Colloid Interface Sci.* **1984**, 102, 146.
- (17) Nagtegaal, M.; Stroeve, P.; Ensling, J.; Gütlich, P.; Schurrer, M.; Voit, H.; Flath, J.; Käshammer, J.; Knoll, W.; Tremel, W. *Chem.—Eur. J.* **1999**, 5, 1331.
- (18) XRD measurement alone is not sufficient to establish the iron oxide phase as XRD peaks of magnetite are almost undistinguishable from those of maghemite, which is formed by oxidation of magnetite.
- (19) Dormann, J. L.; Fiorani, D.; Tronc, E. *Adv. Chem. Phys.* **1997**, 98, 283.
- (20) Gittleman, J. I.; Abeles, B.; Bozowski, S. *Phys. Rev. B* **1974**, 9, 3891.
- (21) Vassiliou, J. K.; Mehrotra, V.; Russell, M. W.; Giannelis, E.; McMichael, R. D.; Shull, R. D.; Ziolo, R. F. *J. Appl. Phys.* **1993**, 73, 5109.
- (22) Dormann, J. L.; Bessois, L.; Fiorani, D. *J. Phys. C* **1988**, 21, 2015.
- (23) Fiorani, D.; Dormann, J. L.; Cherkaoui, R.; Tronc, E.; Lucari, F.; D'Orazio, F.; Spinu, L.; Nogues, M.; Garcia, A.; Testa, A. M. *J. Magn. Magn. Mater.* **1999**, 196, 143.
- (24) (a) Palacin, S.; Hidber, P. C.; Bourgoin, J.; Miramond, C.; Fermon, C.; Whitesides, G. M. *Chem. Mater.* **1996**, 8, 1316. (b) Xue, D.; Zhang, L.; Gao, C.; Xu, X.; Gui, A. *Chin. Phys. Lett.* **2004**, 21, 733.
- (25) (a) Morin, F. J. *Phys. Rev.* **1950**, 78, 819. (b) Zysler, R. D.; Fiorani, D.; Testa, A. M.; Suber, L.; Agostinelli, E.; Godinho, M. *Phys. Rev. B: Condens. Matter Mater. Phys.* **2003**, 68 (21), 212408.